

---

# Dislocation-ledge coupling governs semicoherent precipitate growth

Jin-Yu Zhang<sup>a,b,c</sup>, Juan Du<sup>a,d</sup>, Lin Yang<sup>e</sup>, Frédéric Momprou<sup>d</sup>, Shigenobu Ogata<sup>b\*</sup>,

Wen-Zheng Zhang<sup>a\*</sup>

<sup>a</sup> Key Laboratory of Advanced Materials (MOE), School of Materials Science and Engineering, Tsinghua University, Beijing, 100084, China

<sup>b</sup> Department of Mechanical Science and Bioengineering, The University of Osaka, Osaka, 560-8531, Japan

<sup>c</sup> Department of Physics, McGill University, 3600 University Street, Montréal, Québec, H3A 2T8, Canada

<sup>d</sup> CEMES-CNRS, Université de Toulouse, 29 rue J. Marvig, Toulouse, 31055, France

<sup>e</sup> School of Materials Science and Engineering, Beijing Institute of Technology, Beijing, 100084, China

\* Corresponding authors:

Shigenobu Ogata, Email address: [ogata@me.es.osaka-u.ac.jp](mailto:ogata@me.es.osaka-u.ac.jp)

Wen-Zheng Zhang, Email address: [zhangwz@tsinghua.edu.cn](mailto:zhangwz@tsinghua.edu.cn)

## Abstract

Semicoherent precipitates govern strength, stability and transformation pathways in structural alloys, yet the kinetic defect process underlying their three-dimensional growth has remained unresolved. Here we show that lath growth is driven by diffusion-enabled, non-conservative reorganization of closed interfacial dislocation networks coupled to nanoscale growth ledges. Phase-field-crystal simulations of a model face-centred cubic/body-centred cubic transformation reveal strongly anisotropic kinetics:

---

end faces advance continuously along the long axis, whereas broad facets thicken by discrete ledge sweeps accompanied by mixed glide-climb reactions. O-lattice analysis predicts the defect network, explains the anisotropy through misfit-localization geometry, and shows how the same dislocation motion accommodates transformation strain. In situ transmission electron microscopy of austenite precipitates in duplex stainless steel captures rapid ledge propagation on habit planes, consistent with the predicted mechanism. These results identify the missing kinetic unit of semicoherent precipitate growth and establish a transferable defect-kinetics framework for morphology selection.

## **Introduction**

Precipitation strengthening underpins the performance of many structural alloys, where precipitate size, shape and spatial distribution set the strength–ductility balance and long-term microstructural stability<sup>1, 2</sup>. In technologically important systems—including steels, Ti alloys, and Zr alloys—precipitates are commonly bounded by semicoherent interfaces: lattice misfit is accommodated by dense arrays and networks of interfacial dislocations<sup>3-9</sup>. Because these dislocations must move and reorganize as the interface advances, semicoherent interface migration is inherently defect-mediated and frequently produces highly anisotropic growth, such as rapid lengthening but slow thickening<sup>10</sup> that culminates in plate-, needle- or lath-like (Widmanstätten-type) morphologies<sup>11</sup>. Yet despite decades of crystallographic and microscopic study, a predictive kinetic description of how semicoherent precipitates grow in three

---

dimensions is still missing. In particular, the defect process that links interfacial dislocations, growth ledges and sustained interface migration has remained unresolved.

Experiments have established that semicoherent interfaces around lath precipitates are structurally heterogeneous<sup>12, 13</sup>. Many precipitates develop a long axis lying within dominant facets—typically a habit plane and one or more side facets<sup>3-6, 8, 14-16</sup>—where misfit is accommodated by periodic arrays of interfacial dislocations. By contrast, end faces that are normal or inclined to the long axis often appear curved and exhibit more complex dislocation networks<sup>7, 17</sup>. Nanoscale growth ledges<sup>18</sup> have been reported on semicoherent interfaces across steels<sup>3</sup>, Ni/Cu-based alloys<sup>14, 19-21</sup> and Ti/Zr-based alloys<sup>6, 8, 9, 22</sup>, and are widely invoked to rationalize stepwise facet advance. Experimental characterizations (including transmission electron microscopy (TEM)<sup>8, 21, 22</sup> and high-resolution TEM<sup>3, 6</sup>) and crystallographic analyses<sup>23, 24</sup> have resolved ledge character and associated dislocation content in several systems, but these observations remain largely static or local. Direct time-resolved evidence capturing how ledges migrate while coupled to dense interfacial dislocation structures in three dimensions (3D) remains limited. Much of the experimental evidence is indirect—such as changes in ledge positions after short ageing treatments<sup>14</sup>—with only a few in situ studies reporting lateral ledge motion on facets<sup>23</sup>. Several works have further suggested that ledge-mediated migration may involve non-conservative defect processes<sup>6, 20, 23</sup>, but how such processes operate at semicoherent precipitate interfaces, how they couple to interfacial dislocation motion, and how they accommodate transformation strain during sustained growth are still poorly understood. In particular, it is unclear how habit planes,

---

side facets and end faces act together as parts of a single evolving defect system.

Recent in situ atomic-resolution studies at grain boundaries have highlighted that non-conservative defect kinetics—through point-defect-assisted climb and disconnection motion—can govern interface migration<sup>25-28</sup>. These advances suggest that point-defect transport may also contribute to semicoherent precipitate growth as well. Obtaining comparable mechanistic evidence at semicoherent precipitate interfaces is substantially more challenging because it requires adequate spatial resolution at elevated temperatures. Meanwhile, the 3D precipitate geometry and crystallographically complex interfaces complicate the interpretation. Dense interfacial dislocation arrays with nanometre-scale spacing can yield weak or overlapping contrast during dynamic migration, and free surfaces in TEM foils may bias defect behaviour relative to bulk conditions<sup>29</sup>. These constraints motivate complementary approaches that can resolve the coupled evolution of interface structure, migration kinetics and precipitate morphology, while remaining quantitatively testable against experiments.

Atomistic simulations offer powerful mechanistic insight, yet most approaches are constrained either by time scales or by an incomplete treatment of diffusion and non-conservative defect motion, thereby limiting their ability to capture sustained three-dimensional growth of semicoherent precipitates. Molecular dynamics readily resolves conservative defect motion and interface migration coupled to dislocation glide<sup>30-32</sup>, but the accessible time scales and typical driving forces often emphasize shear-dominated responses rather than diffusive-time-scale growth<sup>33</sup>. Lattice-based Monte Carlo<sup>30, 34</sup> approaches can access longer time scales and include diffusion, but commonly treat

---

chemical degrees of freedom on lattice sites and may not naturally capture vacancy sources and sinks or the non-conservative evolution of interfacial dislocation networks. Grand-canonical Monte Carlo can, in principle, enable open-ensemble exchange at interfaces and defects<sup>25</sup>, yet insertion and deletion events remain energetically costly in crystalline structures, limiting efficient sampling of sustained facet advance and ledge propagation. Coarse-grained frameworks that evolve on diffusive time scales while retaining atomistic resolution of crystal symmetry—such as phase-field-crystal (PFC) models<sup>35</sup> that have been applied to various microstructure evolution processes<sup>27, 36, 37</sup>—provide an attractive route to bridge this gap and to connect non-conservative defect kinetics to interface migration modes.

Here we identify the missing kinetic unit of semicoherent precipitate growth by showing that diffusion-enabled non-conservative motion of interfacial dislocations is intrinsically coupled to the nucleation and lateral propagation of nanoscale growth ledges. We combine 3D PFC simulations with crystallographic O-lattice theory and in situ TEM to resolve precipitate growth through semicoherent interface migration in a prototypical FCC/BCC system. The simulations reveal strongly anisotropic growth kinetics: interfaces advance continuously along the lath long axis, whereas facet thickening proceeds intermittently via laterally propagating growth ledges. By tracking the time-resolved evolution of the interfacial defect structure in 3D, we show that interfacial dislocations on the habit plane, side facets and end faces connect into closed loops encircling the precipitate. These loops expand within well-defined loop planes that are generally not crystallographic slip planes, so their motion involves mixed glide—

---

climb and requires point-defect transport. Crystallographic analyses predict the arrangement of interfacial dislocation networks and explain how their non-conservative motion accommodates transformation strain and drives ledge-mediated facet kinetics, leading to a characteristic lath morphology. In situ TEM observations of austenite precipitates in duplex stainless steels capture rapid ledge propagation on habit planes and stepwise interface advance, consistent with the predicted migration mode. Together, these results bridge a long-standing gap between transformation strain accommodation and interface migration mechanisms by linking point-defect transport, dislocation reactions and ledge-mediated migration, and establish a quantitative, transferable framework for morphology selection in defect-mediated phase transformations.

## Results

### PFC simulations of semicoherent precipitate growth

Starting from a spherical FCC nucleus embedded in a BCC matrix with a selected variant of Kurdjumov-Sachs (K-S) orientation relationship, the precipitate rapidly evolves into a lath morphology bounded by broad habit planes, narrow side facets, and curved end faces (Fig. 1 and Supplementary Movie 1), with a long axis aligned with the parallel close-packed directions,  $[0\bar{1}1]_f \parallel [1\bar{1}1]_b$ . Both the habit planes and side facets remain semicoherent, accommodating misfit via periodic interfacial dislocation arrays with Burgers vectors of  $\mathbf{b}_1 = [0\bar{1}1]_f/2|[1\bar{1}1]_b/2$  and  $\mathbf{b}_2 = [10\bar{1}]_f/2|[1\bar{1}1]_b/2$ , respectively. At the end face,  $\mathbf{b}_1$  and  $\mathbf{b}_2$  segments intersect, and at some junctions, small segments of a third Burgers vector,  $\mathbf{b}_3 = \mathbf{b}_1 + \mathbf{b}_2 = [1\bar{1}0]_f/$

$2[100]_b$ , are present. The resulting key features, including lath shape with a long-axis, the two major facets, and interfacial dislocation structures (Burgers vectors, line directions, and dislocation spacings), are in principle consistent with reports on lath austenite precipitates in duplex stainless steels<sup>5</sup>, and lath Cr precipitate in Cu-<sup>16, 21</sup> and Ni-based alloys<sup>20</sup> (Table S1). Minor deviations from experiments mainly arise from the idealized lattice-parameter ratio ( $a_f/a_b = \sqrt{3/2}$ ) adopted in the structural PFC model. This enforces an exact match between the Burgers-vector magnitudes and the close-packed plane spacings of the FCC and BCC lattices, respectively. In real alloys, small mismatches in these quantities can introduce slight angular deviations in the precipitate long axis and facet orientations, plus additional coarse-spaced misfit dislocations on side facets<sup>15, 19, 20</sup>.

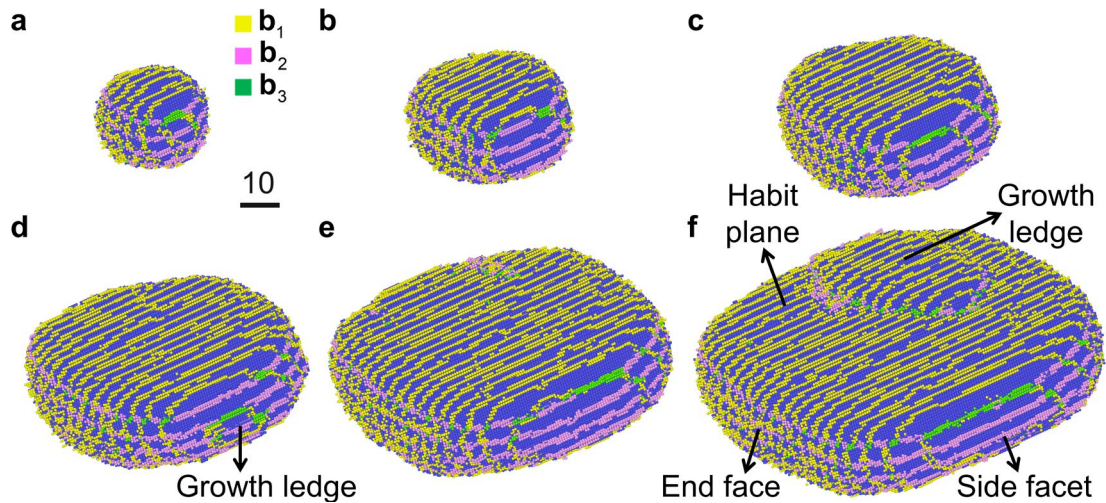


**Fig. 1 Growth process of the FCC precipitate in the BCC matrix.** Atoms belonging to the FCC phase are shown in blue. Atoms at the dislocation cores with different Burgers vectors are coloured distinctly ( $b_1$ ,  $b_2$ ,  $b_3$ ). For visual clarity, atoms in the surrounding BCC matrix are not shown. Length and time are given in dimensionless units of the PFC model.

---

The lath morphology arises from strongly mode-dependent migration of the interfaces surrounding the precipitate. Despite carrying a dense dislocation network, the end face advances rapidly and continuously along the long axis. In contrast, the side facet and habit plane migrates intermittently via a ledge mechanism (Supplementary Movie 1): a semicoherent ledge nucleates on the facet and propagates laterally, accompanied by the formation/expansion of a dislocation loop on the ledge risers. Ledge propagation is also highly anisotropic—nearly continuous parallel to the long axis but proceeding via kink nucleation and propagation in the transverse direction. Each ledge sweep advances the corresponding facet by one ledge height and translates the associated interfacial dislocation array accordingly. When a ledge reaches a facet junction, its riser is absorbed into the neighbouring facet and the end face, thereby contributing to both lath thickening and widening. The PFC-predicted ledge is consistent with the growth ledges reported on semicoherent FCC/BCC facets in multiple alloy systems, with a typical height of 1 nm<sup>14, 15, 19</sup>.

Taken together, interfacial dislocations on the habit planes, side facets, and end faces connect into closed loops encircling the precipitate, consistent with previous interpretations of semicoherent precipitate interfaces<sup>7, 21</sup>. By tracking their time-resolved evolution, our simulations further show that these loops expand within well-defined loop planes that act as the effective shear planes for interfacial dislocation motion. Specifically,  $\mathbf{b}_1$  dislocations on the habit planes and end faces close into loops whose loop plane is parallel to the side facet, whereas  $\mathbf{b}_2$  dislocations on the side facets and end faces form loops parallel to the habit plane. Because the semicoherent facets in

---

real materials are usually irrational, the loop planes are generally not typical slip planes, so loop expansion often proceeds by mixed glide-climb motion and requires atomic diffusion. For example, the Burgers vector of  $\mathbf{b}_2$  is inclined by  $\sim 22^\circ$  relative to its loop plane, implying a climb component during advance. Consistently, Fig. S2 shows that during the ledge sweep across the side facet,  $\mathbf{b}_2$  dislocations undergo non-conservative motion with a negative climb component, as expected when BCC transforms into the denser FCC structure. Overall, the simulation provides the 3D, time-resolved view that links non-conservative interfacial dislocation motion to facet/end-face migration modes and, ultimately, to the emergence of the Widmanstätten-type lath morphology widely observed in structural alloys.

### **In-situ TEM observations**

To examine whether the growth-ledge-mediated advance inferred from simulations occurs on real FCC/BCC interfaces, we performed in situ TEM heating and tracked the habit plane migrations of freshly formed austenite precipitates in ferrite matrix, which exhibit long axes approximately aligned in the TEM foil (Fig. S3). The habit plane advanced in a mixed mode: discrete growth ledges traversed laterally along the long axis, while a concurrent, apparently ledge-free normal drift occurred within the experimental time resolution. In a representative event at 745 °C, three nanometre-scale growth ledges (noted 1, 2 and 3 in Fig. 2) were observed to migrate laterally over tens of seconds (Fig. 2a-d and Supplementary Movies 2 and 3), producing stepwise increments in the habit plane position. Ledges were identified by the discontinuity in

---

the thickness fringes along the interface. Between ledge passages, the interface continued to migrate forward normally, indicating an additional contribution to advance beyond resolvable ledge motion. Frame-difference images (Fig. 2e,f) isolate this behaviour and reveal a measurable net normal displacement accumulated during the intervals between successive ledge passages. Quantitatively, by averaging over the events shown in Fig. 2e,f, the lateral ledge-motion rate along the long axis is substantially higher than the averaged normal advance ( $\sim 10$  nm/s versus  $\sim 1.2$  nm/s in this case), consistent with strongly direction-dependent kinetics of habit-plane migration and with the anisotropic ledge propagation resolved in the simulations.

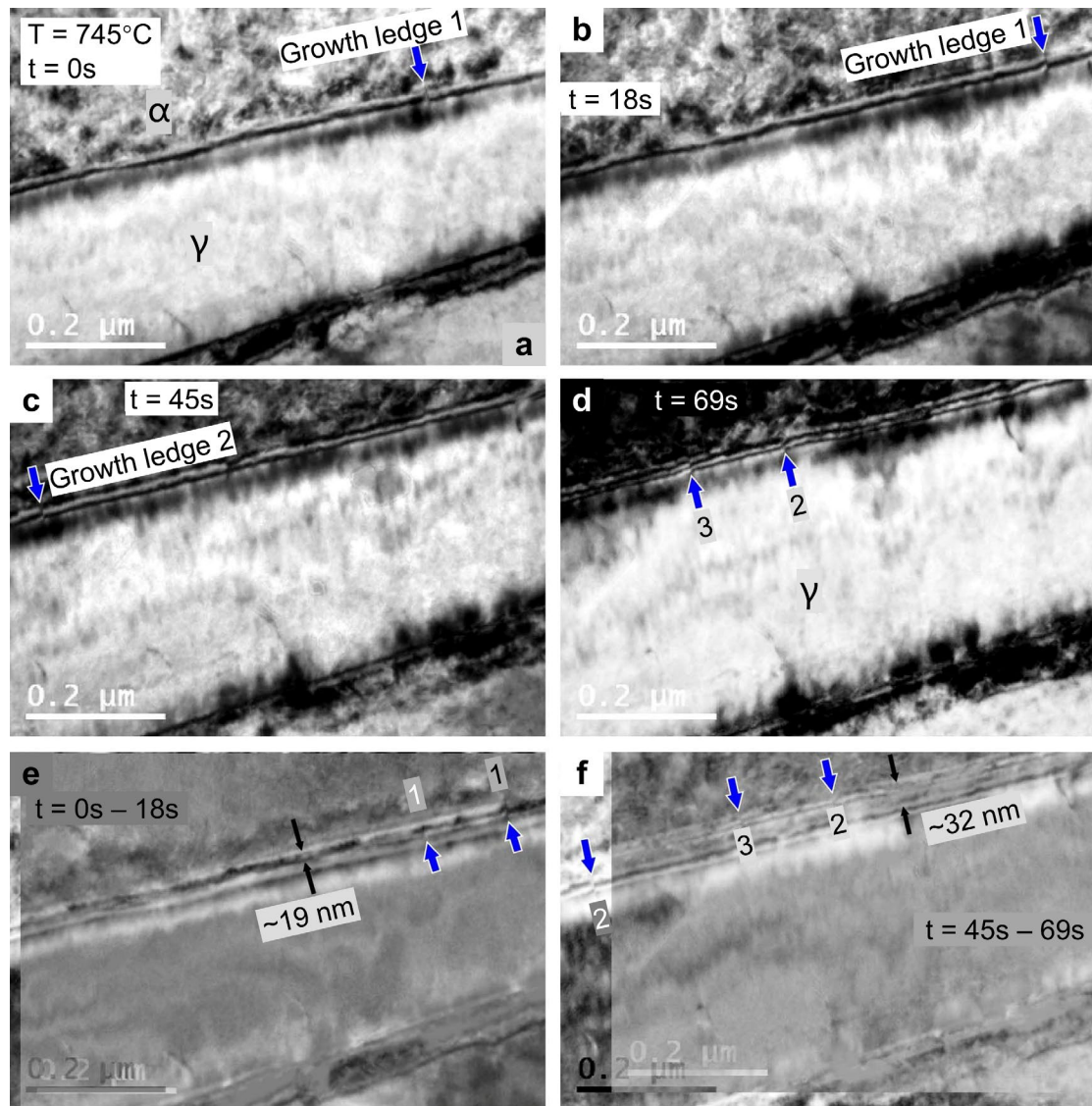


**Fig. 2 Mixed-mode migration of an austenite/ferrite habit plane during in situ TEM heating.** **a–d** Sequential frames at 745 °C showing three growth ledges (blue arrows) gliding laterally along the habit plane, approximately parallel to the long axis of the austenite precipitate. **e–f** Frame-difference images between **a, b**, and **c, d**, respectively, highlighting the net normal advance (black arrows) of the habit plane between ledge passages. Image displacements during the experiment are corrected using surface fiducial markers.

At a second habit plane captured at higher magnification (Fig. 3a–e and Supplementary Movie 4), the projected component of normal migration can be quantified more directly. Besides the lateral passage of discrete growth ledges, frame difference images reveal a fluctuating, ledge-free normal drift of the interface whose

---

magnitude varies from one time window ( $\sim 0.1$  nm/s, Fig. 3f) to another ( $\sim 0.8$  nm/s, Fig. 3g). Such fluctuations might result from transient pinning by local heterogeneities in the TEM foil. When a growth ledge is resolved (Fig. 3e), the corresponding difference image (49–63 s) reveals a clear spatial contrast in the normal advance (Fig. 3h): regions swept by the ledge have advanced by  $\sim 2$  nm in projection, whereas adjacent regions not swept by the ledge have advanced by  $\sim 1$  nm over the same time window. The difference ( $\sim 1$  nm) therefore provides an estimate of the ledge step height, superposed on a concurrent ledge-free normal drift. Together, these observations indicate that habit-plane advance comprises (i) growth-ledge-mediated, stepwise increments superposed on (ii) a concurrent normal drift that can proceed without a clearly resolvable ledge front at the current spatiotemporal resolution.

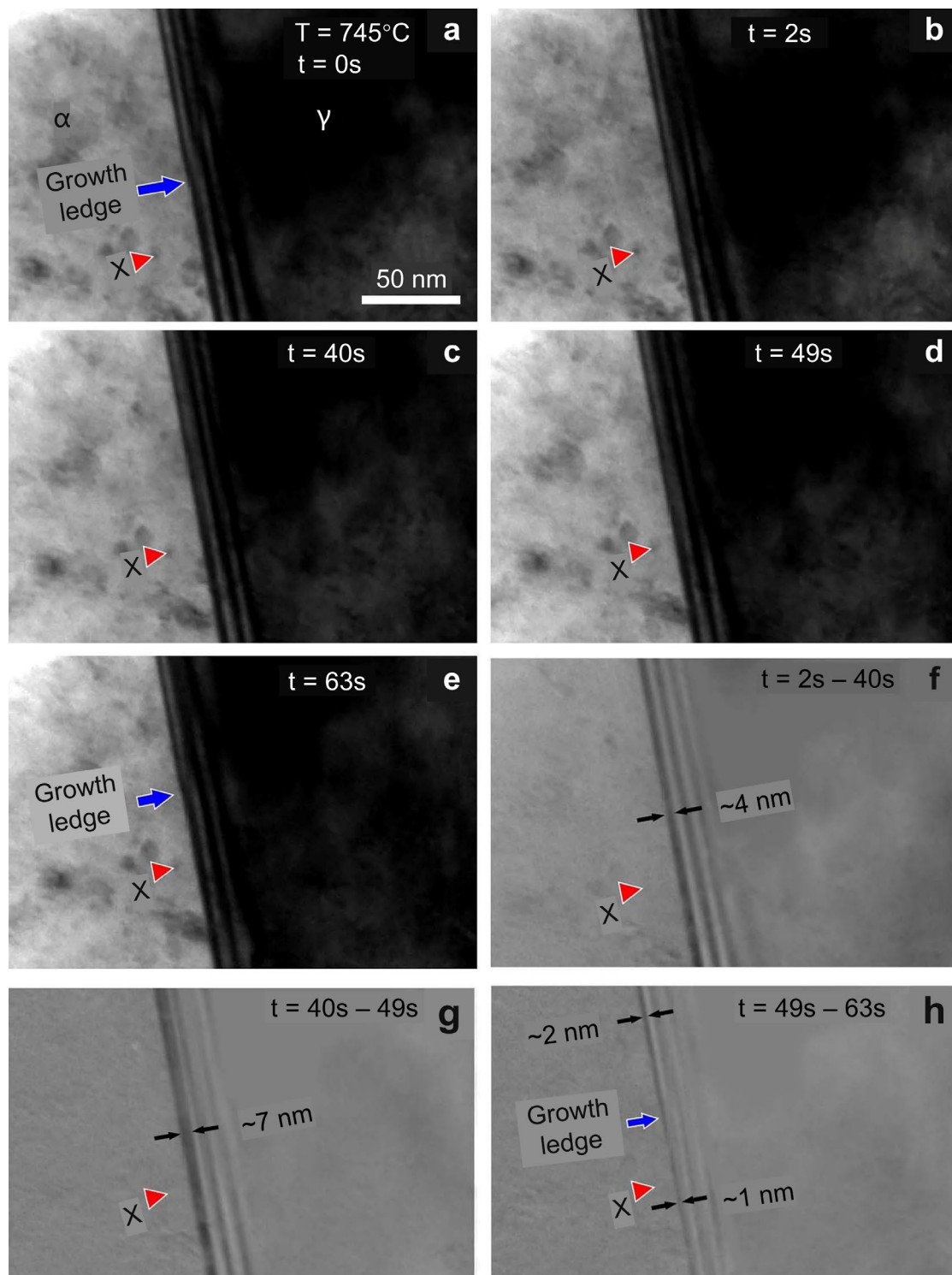


**Fig. 3 Habit-plane advance resolved at higher magnification.** **a–e** Sequential frames at  $750^\circ\text{C}$  showing the normal motion of an austenite/ferrite habit plane and lateral passage of a growth ledge (blue arrow). **f–g** Frame difference images for two ledge-free intervals, highlighting measurable normal displacements of the habit plane with different magnitudes. **h** Frame difference image for an interval containing a growth ledge passage, revealing an additional discrete normal increment associated with the ledge height.

---

## Discussion

To interpret the interfacial defect structures that emerge during lath growth, we analysed the semicoherent FCC/BCC interfaces using O-lattice theory<sup>38</sup>. In the long-axis projection (Fig. 4a), the edge-on O-lines (centres of coherent patches) and O-cell walls (loci of concentrated misfit) define an ordered misfit-localization pattern whose intersections with the habit plane, side facet and end face predict the observed interfacial dislocations of  $\mathbf{b}_1$  arrays,  $\mathbf{b}_2$  arrays, and a network of  $\mathbf{b}_1$ ,  $\mathbf{b}_2$ , and  $\mathbf{b}_3$  segments, respectively. The close agreement between this geometric construction (Fig. 4a) and the defect cores resolved in the 3D PFC simulations (Fig. 4b,c) and experimental observations (Fig. 4d) indicates that the dislocation network is not an incidental consequence of growth, but is largely prescribed by the crystallographic distribution of misfit. Extending the O-cell-wall construction to the full 3D precipitate (Fig. 5) further predicts a closed interfacial network in which segments on different interfaces connect across edges. The simulations show that this network is not static: during ledge nucleation and propagation on semicoherent facets it undergoes systematic reactions, including splitting and recombination of segments on the ledge risers, consistent with the O-lattice-based construction (Fig. 5 and Fig. S4). In this way, the geometric misfit framework not only predicts the defect arrangement, but also provides a theoretical basis for the defect reactions that accompany growth.

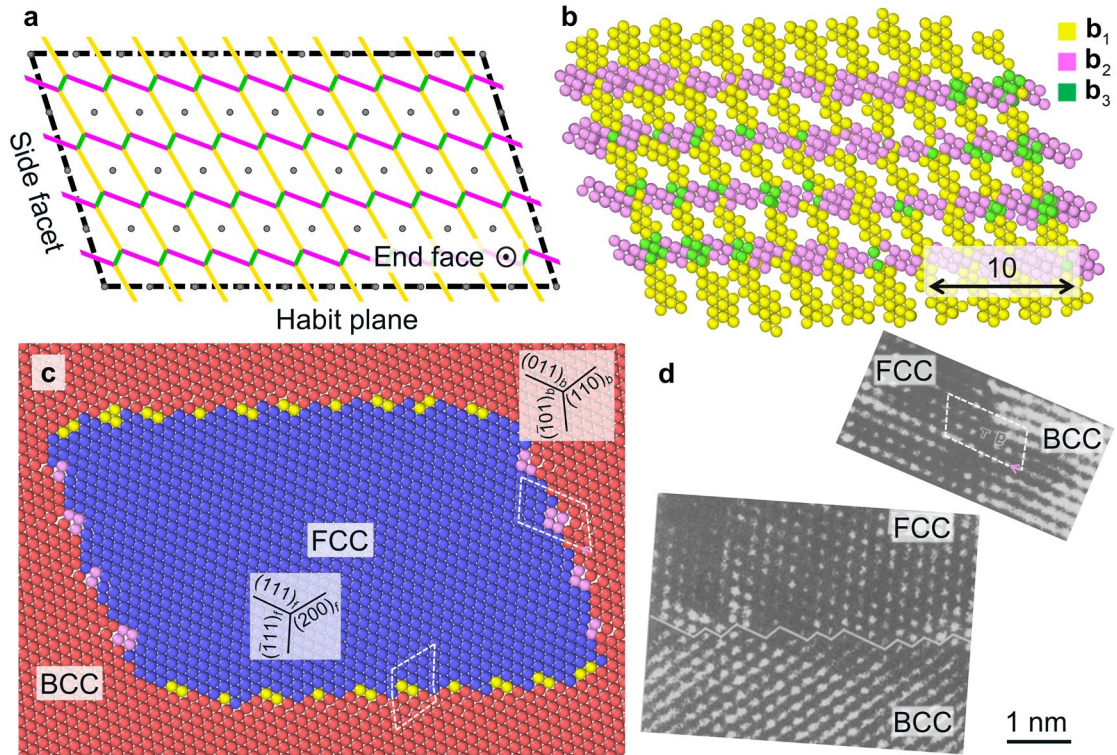


**Fig 4. O-lattice prediction and PFC-resolved interfacial dislocations viewed along the long axis.** **a** O-lattice construction viewed from the long axis: grey dots mark edge-on O-lines and coloured segments indicate edge-on O-cell walls associated with different Burgers vectors; dashed lines outline the traces of the habit plane and side facet, while the end-face region is nearly normal to the long axis. **b** PFC snapshot showing the corresponding interfacial dislocation network. All the atoms inside the crystals are removed. **c** The cross-sectional view of the precipitate. Atoms in FCC and BCC are coloured blue and red, respectively. **d** High-resolution image of the FCC/BCC habit plane and a dislocation core on the side facet, reproduced from Furuhashi et al<sup>19</sup>. In **c**, the  $b_1$  dislocation core appears invisible by a 2D Burgers circuit because of no in-plane Burgers vector component.

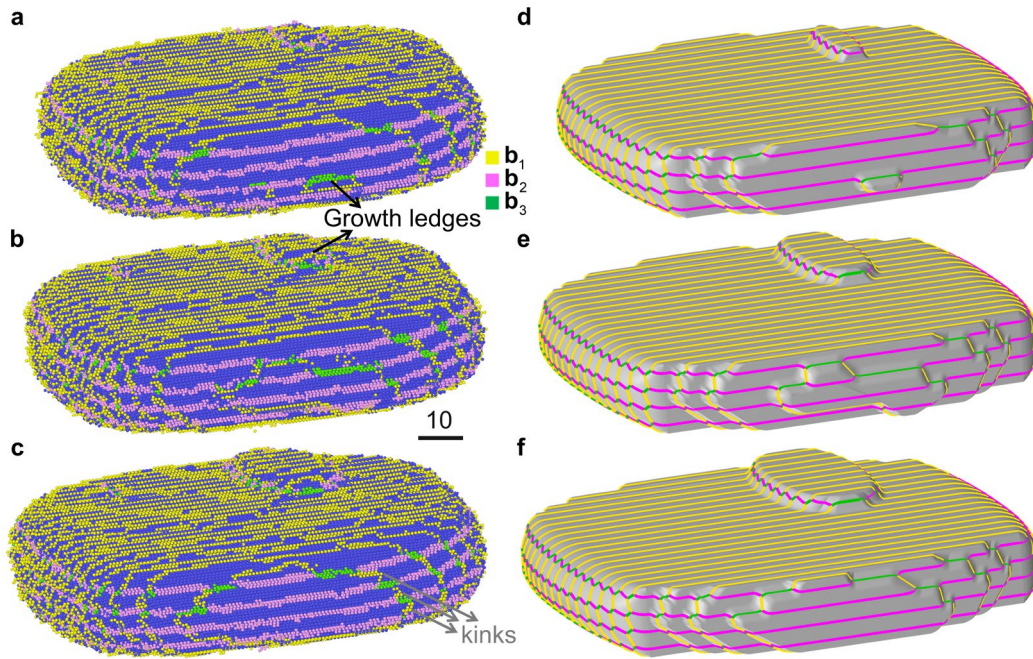


**Fig 5. Growth ledge nucleation and propagation on semicoherent precipitate facets.** **a–c** PFC snapshots showing the nucleation and lateral propagation of growth ledges on both side facet and habit plane; **d–f** Corresponding 3D dislocation network calculated by the O-lattice theory, taking the interface geometry from the simulated precipitate. Dislocations are shown in different colours according to the Burgers vectors.

The same picture explains the pronounced anisotropy of the interface kinetics. Along the lath long axis, which corresponds to an invariant or no-misfit direction in the present geometry, the O-cell walls define a continuous set of equivalent low-resistance sites. By contrast, motion normal to the long axis requires dislocations to move across the discrete O-cell-walls; departures from planes of periodic O-lines generate an increasing misfit strain and therefore a high lattice resistance<sup>39</sup> to be released by dislocation nucleation. This difference rationalizes why the end face can advance rapidly and approximately continuously along the long axis, while facet thickening is expressed through semicoherent growth ledges and their associated kinks. The ledge is therefore not merely a geometric surface step, but the mesoscale expression of how the closed interfacial dislocation network reorganizes under anisotropic resistance imposed by the

---

underlying misfit geometry. This interpretation is consistent with the time-resolved PFC results, in which the side facet migrates through semicoherent ledges whereas the end face advances much more smoothly, despite both regions carrying dense interfacial defects. More broadly, this O-lattice-based geometric analysis of growth ledges is not restricted to the idealized lattice-parameter ratio used in the structural PFC model. It can be directly instantiated using experimental lattice parameters, enabling system-specific predictions of growth ledge structures and dislocation arrangements, as shown in our prior study<sup>24</sup> and examples in Supplementary Materials.

The uncovered interfacial processes also resolve a longstanding kinematic question: how lath growth accommodates the transformation strain without requiring extensive long-range plasticity in the surrounding matrix. Classical displacement decompositions identify the shears needed to cancel the transformation distortion by  $\mathbf{T} = \mathbf{b}_{I\alpha}\Delta\mathbf{g}_I^T + \mathbf{b}_{II\alpha}\Delta\mathbf{g}_{II}^T + \mathbf{b}_{III\alpha}\Delta\mathbf{g}_{III}^T$ <sup>40</sup>, where  $\mathbf{T}$  defines transformation displacement matrix the shear plane  $\Delta\mathbf{g}_i^T = \mathbf{g}_{i\gamma}^T\mathbf{T} = \mathbf{g}_{i\gamma}^T - \mathbf{g}_{i\alpha}^T$  ( $i = I, II, III$ ) is the difference between corresponding reciprocal vectors of the product ( $\gamma$ ) and parent ( $\alpha$ ) lattices and  $\mathbf{g}_{i\alpha}^T\mathbf{b}_{j\alpha} = \delta_{ij}$ . For lath-shaped precipitates, the  $\Delta\mathbf{g}_i$  vectors are known to be the normals of the observed facets<sup>4, 5, 8, 9, 12, 17</sup>. In our PFC simulation geometry, under an idealized lattice parameter ratio, the transformation-strain accommodation is effectively dominated by two dislocation shears ( $\mathbf{b}_1$  and  $\mathbf{b}_2$ ) on the facets. However, this theoretical decomposition do not specify how those shears are dynamically delivered when the relevant interface planes are generally irrational and not crystallographic slip planes. Here, the simulations provide that missing link. As the precipitate grows, interfacial dislocations

---

on the habit plane, side facet and end face connect into closed loops whose loop planes are consistent with the required shear-plane geometry. Because the Burgers vectors are generally inclined to these loop planes, loop expansion cannot proceed by glide alone; instead it involves mixed glide–climb and therefore point-defect transport. This non-conservative character is directly evident in the side-facet ledge process, where interfacial dislocations acquire a climb component concurrent with interface migration (Fig. S2). The key implication is that transformation-strain accommodation and interface migration are not separate problems: they are accomplished simultaneously by the same closed dislocation network through diffusion-enabled loop reorganization.

These results clarify how the present mechanism fits within broader classifications of interface migration. One distinction concerns whether migration is conservative or non-conservative<sup>41</sup>, that is, whether point-defect transport is required. A second concerns how the interface advances geometrically, either by apparently continuous normal motion or by lateral step propagation<sup>39</sup>. Recent atomistic studies have clarified the conservative limit<sup>30-32</sup>, in which interface motion is largely glissile and diffusion-free; the present work establishes the complementary non-conservative limit for a 3D semicoherent precipitate interface containing a closed dislocation network. In situ TEM further suggests an intermediate behaviour on real habit planes, where discrete ledge passage is superposed on an apparently ledge-free normal drift within the present spatiotemporal resolution, likely facilitated in thin foils by surface strain relaxation. Our results show that these distinctions are related but not equivalent. The growth process resolved here lies in the non-conservative regime, yet different parts of the same

---

precipitate express that regime through different local migration modes (Fig. 6): the end face advances predominantly in an apparently continuous manner, whereas the habit plane and side facet migrate mainly through ledges. Viewed in this way, habit planes, side facets and end faces are not independent interface regions, but coupled parts of a single evolving defect system. Growth ledges are therefore not merely geometric surface steps, but the mesoscale manifestation of how the closed interfacial dislocation network reorganizes under anisotropic resistance imposed by the periodic misfit geometry. Taken together, these results suggest a hierarchical picture of semicoherent precipitate growth in which point-defect transport (point-defect level) regulates interfacial dislocation reactions (line-defect level, Fig. 6b,c), those reactions determine the local planar mode of advance, and the accumulated local modes shape the evolving lath morphology (Fig. 6a) and its strain accommodation (bulk level). This framework provides a basis for future atomistic modelling of semicoherent interface migration across conservative and non-conservative regimes, and across the crossover between ledge-mediated and apparently continuous advance.

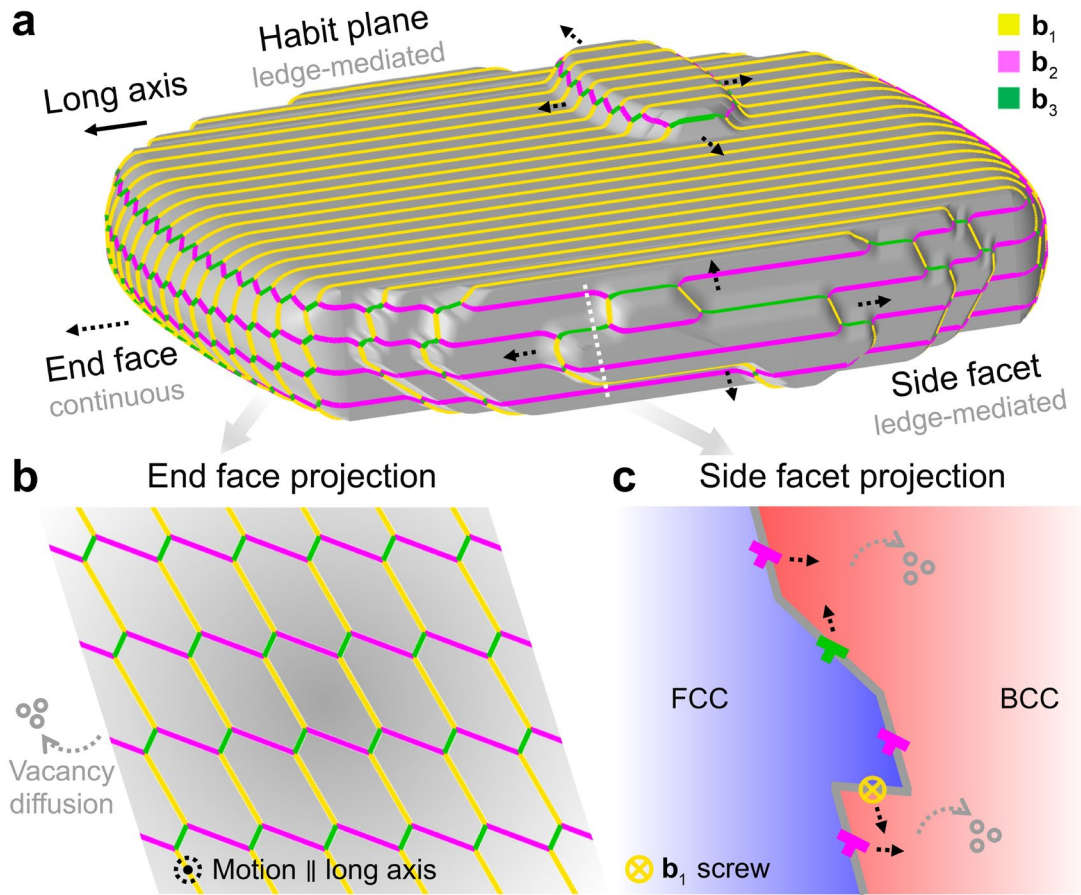


**Fig 6. Hierarchical summary of non-conservative interface migrations during lath precipitate growth.** **a** Schematics of the migration modes of different interface regions surrounding a lath-shaped precipitate (bulk level), which is formed by continuous advance of end face and ledge-mediated migration of habit plane and side facet (planar-defect level). **b** Continuous motion of dislocation networks (line-defect level) on the end face along the long axis (normal to the page), enabled by vacancy diffusion (point-defect level). **c** Mixed dislocation motion during growth ledge migration on the side facet, also enabled by vacancy diffusion. The growth ledge trace in **c** is obtained by slicing in the position indicated by dashed line in **a** and viewed along the long axis.

## Methods

### Phase-field-crystal model

We employed the structural PFC model developed by Greenwood et al.<sup>42, 43</sup> to simulate phase transformations in an FCC/BCC system. The state variable is the dimensionless atomic density field  $n(\mathbf{r})$ . The free-energy functional takes the form<sup>43</sup>:

$$F = \int d\mathbf{r} (n(\mathbf{r})^2/2 - \eta n(\mathbf{r})^3/6 + \chi n(\mathbf{r})^4/12) - \int d\mathbf{r} \int d\mathbf{r}' n(\mathbf{r}) C_2(|\mathbf{r} - \mathbf{r}'|) n(\mathbf{r}')/2, \quad (1)$$

---

where the first term is a local Landau-type polynomial expansion around a uniform reference state, and the second term introduces crystallographic order through the two-body correlation kernel  $C_2(|\mathbf{r} - \mathbf{r}'|)$ . Following Greenwood et al.,  $C_2$  was constructed in reciprocal space as an envelope of Gaussian peaks<sup>42, 43</sup>:

$$C_2^i(k) = \exp(-\sigma^2/\sigma_{Mi}^2) \exp(-(k - k_i)^2/2\alpha_i^2), \quad (2)$$

where  $k_i$ ,  $\alpha_i$ , and  $\sigma_{Mi}$  control the peak position, width, and the dependence on the effective-temperature parameter  $\sigma$ , respectively. To stabilize the FCC phase with a dimensionless lattice parameter  $a_f = \sqrt{3}/2$ , two peaks were used at  $k_1 = 2\sqrt{3}\pi/a_f$  and  $k_2 = 4\pi/a_f$ , corresponding to  $\{111\}_f$  and  $\{200\}_f$  plane families, respectively. Under this parameterization, the BCC lattice parameter satisfies  $a_b = 2\sqrt{2}\pi/k_1 = 1$  because the first peak corresponds to  $\{110\}_b$ . The bulk free-energy densities of the FCC and BCC phases were evaluated as a function of the effective-temperature parameter  $\sigma$  following the method in a prior study<sup>42</sup> (Fig. S1), which identifies the phase-stability crossover used to select transformation conditions.

The density field  $n(\mathbf{r})$  evolved according to conserved dynamics<sup>35</sup>:

$$\partial n(\mathbf{r})/\partial t = \nabla^2[\delta F/\delta n(\mathbf{r})] + \xi, \quad (3)$$

where  $\xi$  represents conserved Gaussian coloured noise subject to a high-frequency cutoff, which filters out unphysical fluctuations with wavelengths shorter than the atomic spacing<sup>37</sup>. This equation conserves the spatial integral of  $n(\mathbf{r})$  and enables evolutions on diffusive timescales within the PFC framework. Time integration was performed in reciprocal space using a semi-implicit Fourier-spectral scheme. The dimensionless grid spacing and time step were  $dx = 0.125$  and  $dt = 0.001$ ,

---

respectively. Simulations were carried out in a fixed box of  $1152 \times 648 \times 432$  grid points under fully periodic boundary conditions. We emphasize that the structural PFC simulations are used here to elucidate the coupled dislocation-ledge mechanism and the geometry-governed interface dynamics, rather than to quantitatively calibrate the dimensionless PFC time to experimental absolute time scales.

### **Initialization and analysis workflow**

The initial configuration consisted of a spherical FCC precipitate embedded in a BCC matrix, with a dimensionless radius of 10 to suppress capillarity-driven shrinkage. The initial orientation relationship was set to the K-S orientation relationship with the variant  $[0\bar{1}1]_f \parallel [1\bar{1}1]_b$  and  $(111)_f \parallel (011)_b$ . By adopting idealized lattice parameters ( $a_f = \sqrt{3/2}a_b$ ),  $[0\bar{1}1]_f/2$  and  $[1\bar{1}1]_b/2$  have identical lengths, and they define the direction of the invariant-line. In addition,  $(111)_f \parallel (011)_b$  define the direction of the invariant-line in reciprocal space. Therefore, three sets of O-lines are solvable for this special case, which simplifies the dislocation structures while retaining the key process of dislocation-mediated ledge mechanism of growth.

After simulation, atomic positions were extracted from the local maxima (density peaks) of  $n(\mathbf{r})$ . Local crystal structures (FCC/BCC/other) were identified using polyhedral template matching (PTM)<sup>44</sup> as implemented in OVITO<sup>45</sup>. Interfacial dislocations were characterized by their spatial distribution and Burgers vectors, determined from the Nye tensor field evaluated on the extracted atomic configuration. The Nye tensor was computed and decomposed using singular value decomposition to

---

obtain the dominant Burgers-vector content<sup>46</sup>.

### **In situ TEM experiments**

A commercial duplex stainless steel with nominal composition Fe-24.9Cr-7.0Ni-3.1Mo (wt%) was used. For in situ observations of freshly nucleated austenite, 10×10×10 mm<sup>3</sup> blocks were encapsulated in evacuated silica tubes and solution-treated at 1300 °C for 30 min, followed by water quenching. TEM foils were prepared from 0.5-mm-thick slices by mechanical thinning and twin-jet electropolishing (Struers Tenupol-3) using 8 vol% perchloric acid in ethanol at 20 V and –30 °C. Immediately before heating experiments, foils were plasma cleaned (Solarus, Gatan; 1 min) to remove hydrocarbon contamination. In situ heating was conducted in a Philips CM20FEG microscope operated at 200 kV using a Gatan double-tilt heating holder. Samples were first heated to 700 °C at the maximum heating rate (~50 °C/min), then heated in 5 °C increments until interface migration or new austenite growth was observed (typically 720–850 °C). Videos were recorded using a Gatan Orius side-entry CCD camera at 15–24 fps, and key frames were extracted for subsequent analysis.

### **Crystallographic calculation of interfacial dislocations**

Interfacial dislocation structures were determined corresponding to the locations of maximal misfit. The O-lattice theory<sup>38</sup> provides a general tool for analysing misfit distribution in any interface. For the K-S orientation relationship considered here, using the special lattice parameter ratio, the misfit at any interface can be accommodated by

---

interfacial dislocations whose Burgers vectors lie within the parallel planes  $(111)_f \parallel (011)_b$ , namely,  $\mathbf{b}_1 = [0\bar{1}1]_f/2|[1\bar{1}1]_b/2$ ,  $\mathbf{b}_2 = [10\bar{1}]_f/2|[11\bar{1}]_b/2$ , and  $\mathbf{b}_3 = [1\bar{1}0]_f/2|[100]_b$ , where symbol “|” denotes corresponding vectors across the transformation. The position of an O-lattice element (position of zero misfit) is defined by a vector,  $\mathbf{x}^o$ , solved from:  $\mathbf{T}\mathbf{x}^o = \sum_i k_i \mathbf{b}_{i\alpha}$ <sup>38</sup>, where  $k_i$  are integers,  $\sum_i k_i \mathbf{b}_{i\alpha}$  indicates any the translational vectors in  $\alpha$  phase.  $\mathbf{T} = \mathbf{I} - \mathbf{A}^{-1}$  is the displacement matrix that links a position  $\mathbf{x}_\gamma$  with its associated displacement  $\mathbf{x}_\gamma - \mathbf{x}_\alpha$ , which are related by  $\mathbf{x}_\gamma = \mathbf{A}\mathbf{x}_\alpha$ . Here,  $\mathbf{A}$  represents the deformation matrix transforming  $\alpha$  lattice to  $\gamma$  lattice. A set of O-cell walls between O-elements corresponds to positions of maximal misfit, are defined by a reciprocal vector,  $\mathbf{c}^o$ , related to a Burgers vector,  $\mathbf{b}_{i\alpha}$ , by  $\mathbf{c}^o = \mathbf{T}^T \mathbf{b}_{i\alpha}/|\mathbf{b}_{i\alpha}|$ <sup>247</sup>. The dislocations are defined by the intersections between the O-cell walls and an interface, and the Burgers vector of the dislocations is  $\mathbf{b}_{i\alpha}$  associated with the particular set of O-cell walls. The interfacial dislocations determined based on the O-lattice theory were employed to compare with PFC-predicted defect structures and experimental observations.

## Data availability

The data that support the findings of this study are available within the Article and its Supplementary Information. Additional data are available from the corresponding author upon reasonable request.

## Code availability

---

The scripts used for data analysis and visualization are available from the corresponding author upon reasonable request.

## References

1. Brown LM, Ham RK. Dislocation-particle interactions. In: *Strengthening methods in crystals* (eds Kelly A, Nicholson RB). Elsevier (1971).
2. Ardell AJ. Precipitation hardening. *Metall. Trans. A* **16**, 2131-2165 (1985).
3. Jiao HS, Aindow M, Pond RC. Precipitate orientation relationships and interfacial structures in duplex stainless steel Zeron-100. *Phil. Mag.* **83**, 1867-1887 (2003).
4. Qiu D, Zhang W-Z. A TEM study of the crystallography of austenite precipitates in a duplex stainless steel. *Acta Mater.* **55**, 6754-6764 (2007).
5. Du J, Momprou F, Zhang W-Z. A TEM study of the crystallography of lath-shaped austenite precipitates in a duplex stainless steel. *J. Mater. Sci.* **52**, 11688-11700 (2017).
6. Furuhashi T, Ogawa T, Maki T. Atomic-structure of interphase boundary of an  $\alpha$ -precipitate plate in a  $\beta$  Ti-Cr Alloy. *Phil. Mag. Lett.* **72**, 175-183 (1995).
7. Zhang Y-S, Zhang J-Y, Zhang W-Z. Dislocation network on the curved end face of  $\alpha$  precipitates in a Ti-8 wt.% Fe alloy. *Phil. Mag.* **102**, 1-14 (2021).
8. Zhang W-Z, Perovic V, Perovic A, Weatherly GC, Purdy GR. The structure of HCP-BCC interfaces in a Zr-Nb alloy. *Acta Mater.* **46**, 3443-3453 (1998).
9. Zhang W-Z, Purdy GR. A TEM study of the crystallography and interphase boundary structure of  $\alpha$  precipitates in a Zr-2.5wt%Nb alloy. *Acta Metall. Mater.* **41**, 543-551 (1993).
10. Kinsman KR, Eichen E, Aaronson HI. Thickening kinetics of proeutectoid ferrite plates in Fe-C alloys. *Metall. Trans. A* **6**, 303 (1975).
11. Ohmori Y, Ohtsubo H, Jung YC, Okaguchi S, Ohtani H. Morphology of bainite and widmanstätten ferrite. *Metall. Mater. Trans. A* **25**, 1981-1989 (1994).
12. Zhang W-Z, Weatherly GC. On the crystallography of precipitation. *Prog. Mater. Sci.* **50**, 181-292 (2005).
13. Howe JM, Pond RC, Hirth JP. The role of disconnections in phase transformations. *Prog. Mater. Sci.* **54**, 792-838 (2009).
14. Chen G, Spanos G, Masumura RA, Reynolds WT. Effects of ledge density on the morphology and growth kinetics of precipitates in a Ni-Cr Alloy. *Acta Mater.* **53**, 895-906 (2005).
15. Luo CP, Weatherly GC. The interphase boundary structure of precipitates in a Ni-Cr alloy. *Phil. Mag. A* **58**, 445-462 (1988).
16. Luo CP, Dahmen U, Westmacott KH. Morphology and crystallography of Cr precipitates in a Cu-0.33 wt% Cr alloy. *Acta Metall. Mater.* **42**, 1923-1932 (1994).

- 
17. Ye F, Zhang W-Z. Dislocation structure of non-habit plane of  $\alpha$  precipitates in a Ti-7.26 wt.% Cr alloy. *Acta Mater.* **54**, 871-879 (2006).
  18. Weatherly GC. The structure of ledges at plate-shaped precipitates. *Acta Metall.* **19**, 181-192 (1971).
  19. Furuhashi T, Wada K, Maki T. Atomic-structure of interphase boundary enclosing BCC precipitate formed in FCC matrix in a Ni-Cr alloy. *Metall. Mater. Trans. A* **26**, 1971-1978 (1995).
  20. Chen JK, Chen G, Reynolds WT. Interfacial structure and growth mechanisms of lath-shaped precipitates in Ni-45 wt% Cr. *Phil. Mag. A* **78**, 405-422 (1998).
  21. Luo CP, Dahmen U. Interface structure of faceted lath-shaped Cr precipitates in a Cu-0.33 wt% Cr alloy. *Acta Mater.* **46**, 2063-2081 (1998).
  22. Furuhashi T, Howe JM, Aaronson HI. Interphase boundary structures of intragranular proeutectoid  $\alpha$  plates in a hypoeutectoid Ti-Cr alloy. *Acta Metall. Mater.* **39**, 2873-2886 (1991).
  23. Zhang J-Y, Zhang Y-S, Momprou F, Zhang W-Z. Structures and migrations of interfaces between  $\beta$  precipitates and  $\alpha'$  matrix in a Ti-2.6 wt% Mo alloy. *Acta Mater.* **281**, 120429 (2024).
  24. Zhang J-Y, Gao Y, Wang Y, Zhang W-Z. A generalized O-element approach for analyzing interface structures. *Acta Mater.* **165**, 508-519 (2019).
  25. Chu S, *et al.* In situ atomic-scale observation of dislocation climb and grain boundary evolution in nanostructured metal. *Nat. Commun.* **13**, 4151 (2022).
  26. Wei J, Feng B, Tochigi E, Shibata N, Ikuhara Y. Direct imaging of the disconnection climb mediated point defects absorption by a grain boundary. *Nat. Commun.* **13**, 1455 (2022).
  27. Qiu C, *et al.* Grain boundaries are Brownian ratchets. *Science* **385**, 980-985 (2024).
  28. Tian Y, *et al.* Grain rotation mechanisms in nanocrystalline materials: Multiscale observations in Pt thin films. *Science* **386**, 49-54 (2024).
  29. Legros M, Momprou F, Caillard D. Observing deformation in situ. *Nat. Mater.* **23**, 20-22 (2024).
  30. Zhang J-Y, *et al.* Dislocation-mediated migration of the  $\alpha/\beta$  interfaces in titanium. *Acta Mater.* **261**, 119364 (2023).
  31. Wang S, Wen T, Han J, Srolovitz DJ. Coherent and semicoherent  $\alpha/\beta$  interfaces in titanium: structure, thermodynamics, migration. *npj Comput. Mater.* **9**, 216 (2023).
  32. Maresca F, Curtin WA. The austenite/lath martensite interface in steels: Structure, athermal motion, and in-situ transformation strain revealed by simulation and theory. *Acta Mater.* **134**, 302-323 (2017).
  33. Thomas SL, Chen K, Han J, Purohit PK, Srolovitz DJ. Reconciling grain growth and shear-coupled grain boundary migration. *Nat. Commun.* **8**, 1764 (2017).
  34. Clouet E, Nastar M, Sigli C. Nucleation of  $\text{Al}_3\text{Zr}$  and  $\text{Al}_3\text{Sc}$  in aluminum alloys: From kinetic Monte Carlo simulations to classical theory. *Phys. Rev. B* **69**, 064109 (2004).
  35. Provatas N, Elder K. *Phase-field methods in materials science and engineering.*

- 
- Wiley-VCH (2010).
36. Mamaev A, Provatas N. Phase-field crystal modeling of lamellar precipitation reactions. *Acta Mater.* **308**, 121978 (2026).
  37. Yang T, *et al.* Non-conservative dynamics of lattice sites near a migrating interface in a diffusional phase transformation. *Acta Mater.* **127**, 481-490 (2017).
  38. Bollmann W. *Crystal defects and crystalline interfaces*. Springer-Verlag (1970).
  39. Cahn JW. Theory of crystal growth and interface motion in crystalline materials. *Acta Metall.* **8**, 554-562 (1960).
  40. Zhang W-Z. Decomposition of the transformation displacement field. *Phil. Mag. A* **78**, 913-933 (1998).
  41. Sutton AP, Balluffi RW. *Interfaces in crystalline materials*. Oxford University Press (1995).
  42. Greenwood M, Ofori-Opoku N, Rottler J, Provatas N. Modeling structural transformations in binary alloys with phase field crystals. *Phys. Rev. B* **84**, 064104 (2011).
  43. Greenwood M, Provatas N, Rottler J. Free energy functionals for efficient phase field crystal modeling of structural phase transformations. *Phys. Rev. Lett.* **105**, 045702 (2010).
  44. Larsen PM, Schmidt S, Schiøtz J. Robust structural identification via polyhedral template matching. *Model. Simul. Mater. Sci. Eng.* **24**, 055007 (2016).
  45. Stukowski A. Visualization and analysis of atomistic simulation data with OVITO-the Open Visualization Tool. *Model. Simul. Mater. Sci. Eng.* **18**, 015012 (2010).
  46. Dai F-Z, Zhang W-Z. An automatic and simple method for specifying dislocation features in atomistic simulations. *Comput. Phys. Commun.* **188**, 103-109 (2015).
  47. Zhang W-Z, Purdy GR. O-lattice analyses of interfacial misfit. I. General considerations. *Phil. Mag. A* **68**, 279-290 (1993).

## Acknowledgements

J.-Y.Z. would like to thank Prof. Nikolas Provatas and Dr. Nana Ofori-Opoku at McGill University for teaching the basic usage of structural PFC codes, and Dr. Rui-Xun Xie for technical assistance in setting up the GPU server used for running PFC simulations. J.-Y.Z. and S.O. acknowledge the funding by projects of JSPS KAKENHI (Grant No. JP23K20037). W-Z.Z. acknowledges the supports from the National Natural Science Foundation of China (Grant No. 51871131) and the National Key Research and

---

Development Program of China (Grant No. 2016YFB0701304). J.-Y.Z. and J.D. acknowledge the China Scholarship Council (No. 201906210309 and No. 201506210313) for funding the stay at McGill University (Canada) and CEMES (France), respectively.

### **Author contributions**

J.-Y.Z. performed simulations and theoretical analyses and wrote the manuscript. J.D. carried out the experiments and analysed the data. L.Y. provided guidance on simulation setup. F.M., S.O., and W.-Z.Z. contributed to the interpretation of the results and revised the manuscript.

### **Competing interests**

The authors declare no competing interests.

## Supplementary Materials

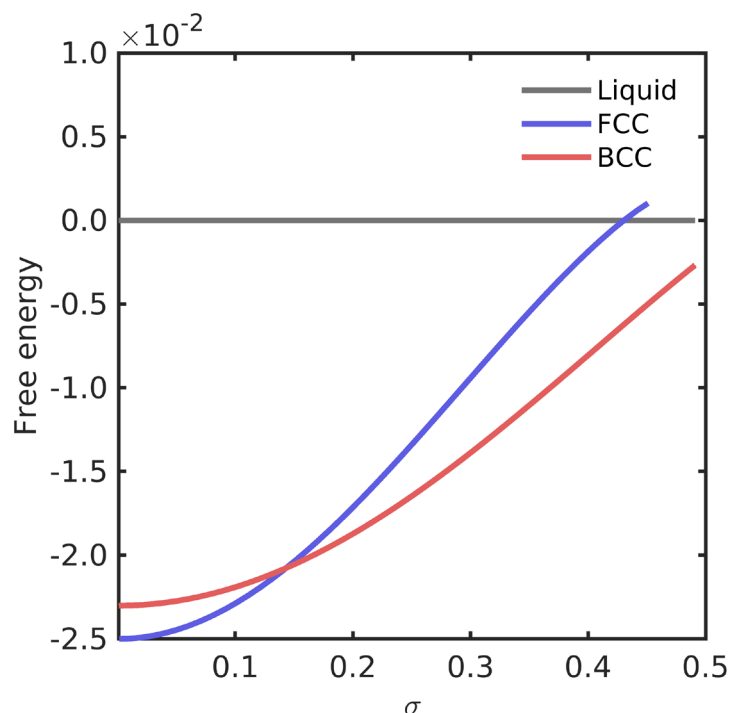


**Fig. S1.** The free energy of FCC and BCC phases with respect to effective temperature  $\sigma$ .

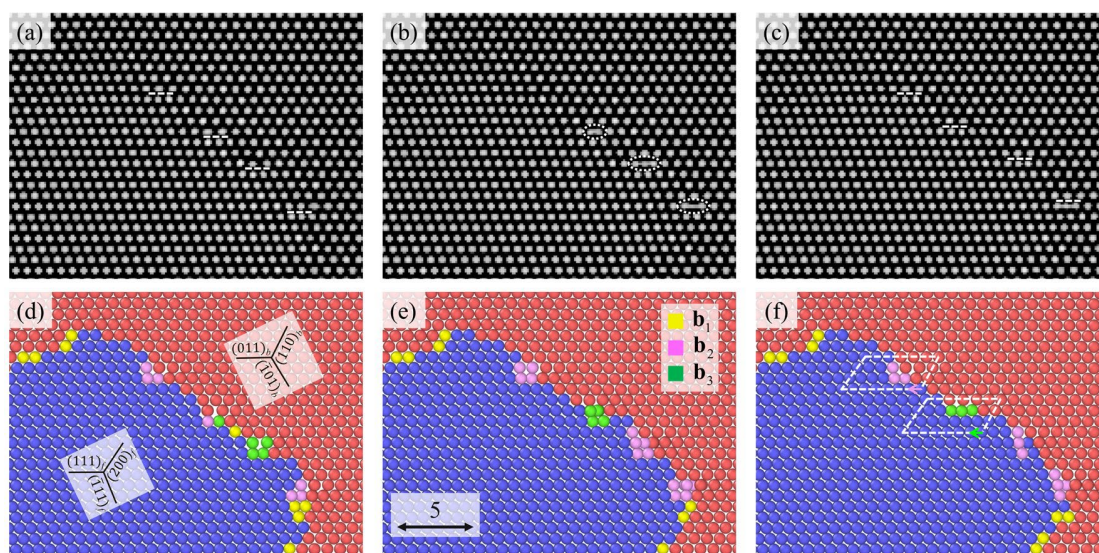


**Fig. S2.** Motion of the dislocation  $b_2$  with climb components during the side facet migration process. **a–c** show the migration and non-conservative motion of three dislocations on the side facet, during which each dislocation moves upward by one atomic plane; the dashed lines indicate the slip planes at each dislocation core. **d–f** present the corresponding atomic configuration of the interface and the associated dislocation structures. The motion of the screw dislocation with Burgers vector  $b_1$  is not visible in **a–c** due to projection effects.

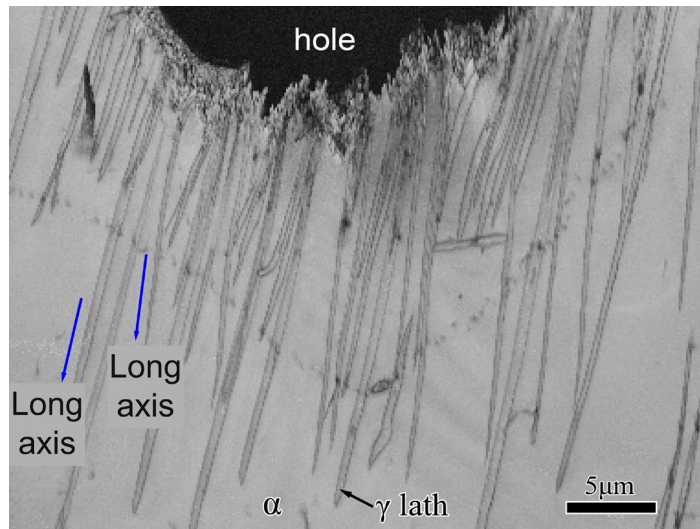


**Fig. S3 Post-mortem overview of newly formed austenite laths after in situ TEM heating.** EBSD band-contrast map acquired near the perforation edge of the electropolished foil after the in situ heating experiment, showing newly formed austenite laths embedded in ferrite matrix. Blue arrows indicate representative long axis directions, revealing that the lath long axes are predominantly aligned within the foil plane.

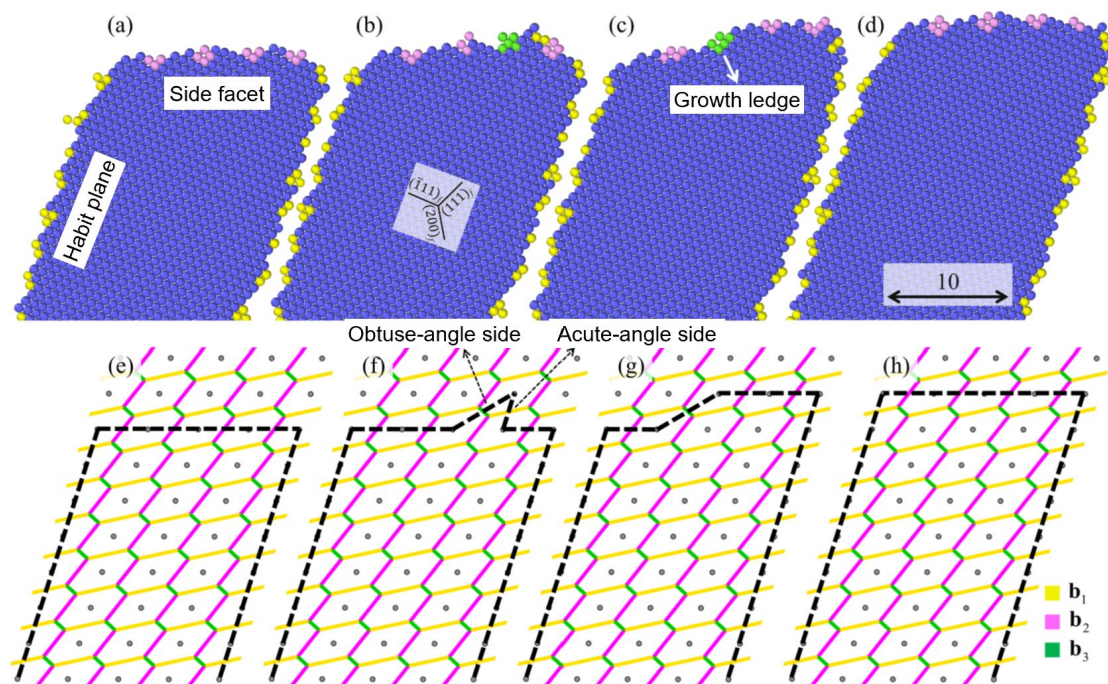


**Fig S4. Cross-sectional views of the nucleation and propagation of a growth ledge on the side facet.** Cross-sections taken on a plane perpendicular to the invariant line. **a–d** PFC snapshots; **e–h** corresponding O-lattice constructions. Grey dots denote edge-on O-lines; coloured segments denote O-cell walls associated with different Burgers vectors. Dashed lines are interface/ledge traces.

**Table S1** Crystallographic features of PFC-predicted lath precipitate and experimentally observed lath precipitates across various alloys

	PFC	Duplex stainless steel <sup>1</sup>	Cu-Cr alloys <sup>2,3</sup>	Ni-Cr alloys <sup>4</sup>
$a_f/a_b$	1.225	1.255	1.264	1.255
OR $\theta_{p-p}(^\circ)$	0	0.45	0	0
$\theta_{d-d}(^\circ)$	0	0.45	0.5	$\leq 0.9$
Long axis	$[0\bar{1}1]_f$	$[0.08\ \bar{0.77}\ 0.64]_f$	$[0.13\ \bar{0.76}\ 0.64]_f$	$[0.06\ \bar{0.76}\ 0.65]_f$
HP $\mathbf{n}_{HP}$	$(2\ 0.8\ 0.8)_f$	$(2\ 1.1\ 1)_f$	$(2\ 1.3\ 1.1)_f$	$(2\ 1\ 1)_f$
$\mathbf{b}_{HP}$	$\mathbf{b}_1$	$\mathbf{b}_1^*$	-	-
$d_{HP}/a_f$	2.4	2.5*	-	-
SF $\mathbf{n}_{SF}$	$(\bar{1}.1\ 2\ 2)_f$	$(\bar{0}.4\ 1.6\ 2)_f$	$(\bar{0}.7\ 2\ 2)_f \sim (\bar{1}.5\ 2\ 2)_f$	$(\bar{0}.5\ 1.9\ 2)_f$
$\mathbf{b}_{SF-fine}$	$\mathbf{b}_2$	$\mathbf{b}_2^*$	-	-
$d_{SF-fine}/a_f$	3.3	3.3*	3.4~4.1	4.1
$\mathbf{b}_{SF-coarse}$	-	$[110]_f/2 [010]_b$	-	-
$d_{SF-coarse}/a_f$	-	26.5	20.5~23.2	32.9

$\theta_{p-p}$ : Angle between  $(111)_f$  and  $(011)_b$ ;  $\theta_{d-d}$ : Angle between  $[0\bar{1}1]_f$  and  $[1\bar{1}1]_b$

OR: orientation relationship; HP: habit plane; SF: side facet;

$\mathbf{n}$ : facet normal;  $\mathbf{b}$ : Burgers vector;  $d$ : dislocation spacing

\* Calculated results based on geometric model

## Comparisons between experimental growth ledges and corresponding geometric constructions in different alloy systems

Using experimental lattice parameters, we calculated the orientation relationship and habit plane structures are using the O-line model<sup>5</sup> implemented in PTCLab<sup>6</sup>. The lattice correspondence between the BCC and FCC phases for the K-S variant considered in this study is:

$$\mathbf{C}_{b \rightarrow f} = \begin{bmatrix} 0.5 & 0.5 & 0 \\ -0.5 & 0.5 & 0 \\ 0 & 0 & 1 \end{bmatrix}.$$

The Burgers vector on the habit plane, i.e.,  $\mathbf{b}_1$ , is taken as the input. Consistent with the

---

experimentally observed orientation relationship in Cu-Cr alloy, the angle between the corresponding Burgers vectors  $\mathbf{b}_1$  in the two phases, i.e.,  $[0\bar{1}1]_f/2$  and  $[1\bar{1}1]_b/2$ , is set as  $0.5^\circ$ .

When the experimental lattice parameters are used,  $[0\bar{1}1]_f/2$  and  $[1\bar{1}1]_b/2$  generally have different magnitudes, and the direct/reciprocal invariant lines can deviate from the close-packed directions. As a result, O-line solutions may not exist for interface planes away from the habit plane. In such cases, we employ a generalized O-element approach developed in our previous work<sup>7</sup>, which enables the determination of coherent regions and interfacial dislocation structures on different interfaces, including side the facets, end faces, and growth-ledges.

Figure S5 compares experimental observations of faceting and interfacial defect structures of a Cr precipitate in a Cu matrix with our geometric calculations. In the previous study<sup>3</sup>, four facets (F1–F4) were identified from TEM observations (Fig. S5a). Periodic ledges with different spacings were reported on facets F2 and F3 (schematically illustrated in Fig. S5b), whereas two families of dislocation arrays with fine and coarse spacings were observed on the curved facet F4. In contrast, dislocations on F1 were not reported, likely because their spacing is too small to produce resolvable contrast under the imaging conditions.

These facet morphologies and defect configurations are reproduced by our generalized O-element construction, in which neighbouring generalized O-elements are connected to form the facets and growth ledges (Fig. S5c). The quantitative comparisons in Fig. S5 and Table S2 demonstrate that the model captures key

crystallographic and geometric features, including facet orientations, ledge spacings/heights on F2 and F3, and dislocation spacings on F4.

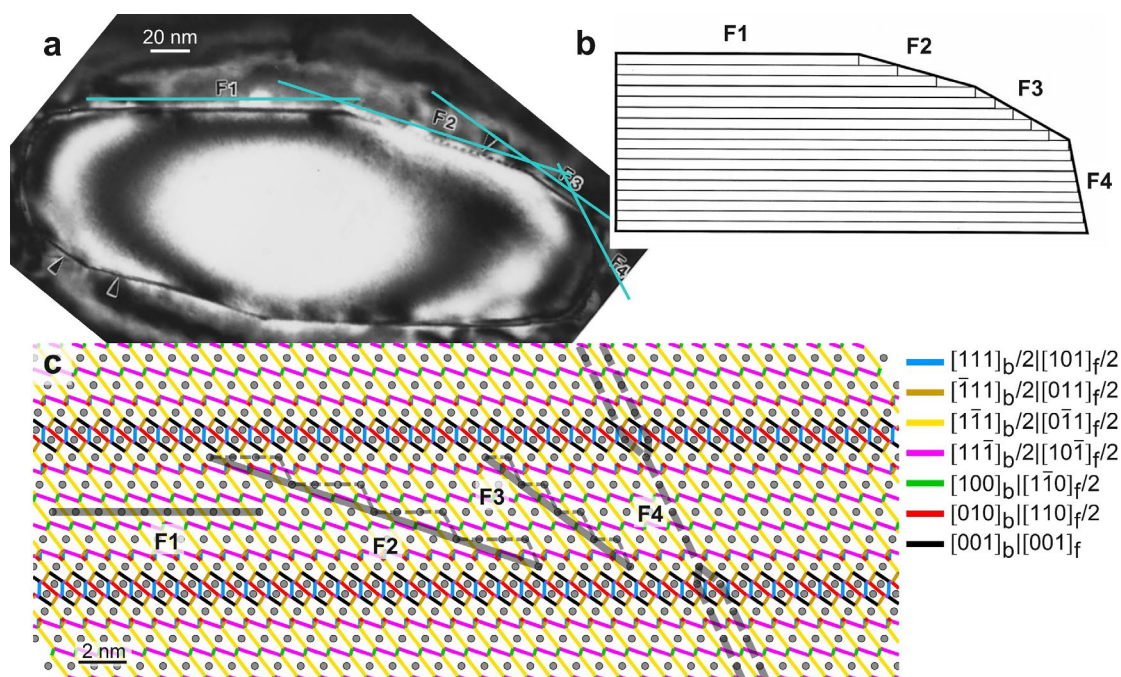


**Fig. S5 Facets and interfacial defect structures of a lath-shaped Cr precipitate in a Cu matrix: experiment vs. geometric construction.** **a** TEM image showing the faceted morphology of the Cr precipitate, with facets F1–F4 indicated. **b** Schematic illustration of the terrace–ledge morphology on facets F1–F4, highlighting the different ledge densities/spacings on F2 and F3. **c** Facets and growth ledges obtained from the generalized O-element construction. Grey dots are edge-on generalized O-lines. Coloured lines denote the Burgers vectors of the O-cell walls (legend). Thick grey lines indicate mean facets orientations and dashed lines on F2 and F3 indicate periodic ledges. The orientations of F4 can vary depending on the choice of coarse-spaced dislocations. The calculated coarse-spaced dislocation on F4 exhibits ledge characters, which are also noted in experiments<sup>3</sup>. **a, b** are reproduced from Luo et al<sup>3</sup>.

**Table S2** Comparison between the experimental and calculated crystallographic features of lath Cr precipitate in Cu matrix

	Exp. <sup>2,3</sup>	Cal.	Dif.
Long axis	$[1 \ -6 \ 5]_f$	$[1.0 \ -6 \ 5.0]_f$	$0.1^\circ$
F1 <b>n</b>	$(5.5 \ 3.5 \ 3.1)_f$	$(5.5 \ 3.4 \ 3.0)_f$	$0.6^\circ$

F2	<b>n</b>	$(1\ 1\ 1)_f$	$(0.88\ 0.98\ 1)_f$	$3.2^\circ$
	$d$ (nm)	3.75	3.74	0.01
F3	<b>n</b>	$(1.6\ 4.1\ 4.6)_f$	$(1.2\ 4.0\ 4.6)_f$	$3.9^\circ$
	$d$ (nm)	1.9	1.94	0.04
F4 (curved)	<b>n</b>	$(-1\ 3\ 3)_{f\sim}$ $(-3\ 4\ 4)_f$	$(-1.2\ 2.3\ 3)_{f\sim}$ $(-2.5\ 2.9\ 4)_f$	$9^\circ$ $8^\circ$
	$d$ (nm)	Fine: 1.25~1.5 Coarse: 7.5~8.5	Fine: 1.39~1.47 Coarse: 6.8~7.3	
	$h$ (nm)	~1.1	1.1	0.0
	$\theta_{p-d}$ ( $^\circ$ )	0	0.5	
	$\theta_{d-d}$ ( $^\circ$ )	0.5	0.5	

$\theta_{p-p}$ : Angle between  $(111)_f$  and  $(011)_b$ ;  $\theta_{d-d}$ : Angle between  $[0\bar{1}1]_f$  and  $[1\bar{1}1]_b$   
**n**: facet normal;  $d$ : dislocation/ledge spacing;  $h$ : smallest ledge height on habit plane

We further demonstrate the applicability of our geometric framework to a different system, namely HCP/BCC interfaces. The required inputs for the O-line model and the generalized O-element approach follow our previous studies<sup>8,9</sup>. In the Ti–7.26Cr alloy, growth ledges with a height of ~10 nm are observed on the habit plane (Fig. S6a, enlarged view), with faint contrast associated with the riser and periodic contrasts on the terrace. These ledge characteristics—including the terrace width, ledge height, and riser orientation—are reproduced by the generalized O-element/O-cell-wall construction (Fig. S6b). In the construction, the terrace (habit plane) contains a periodic array of dislocations, whereas the ledge riser is accommodated by multiple fine-spaced dislocations together with an additional coarse-spaced dislocation. The ledge risers can therefore be regarded as micro side facets; as they accumulate, they form the macroscopic side facet of the precipitate as they accumulate.

Additional, less frequently observed facet configurations can also arise. For example, the alternative side facet (labelled “side facet B” in Fig. S7) is reproduced by choosing a different coarse-spaced dislocations on the side facet, resulting in a distinct facet orientation compared with “side facet A”.

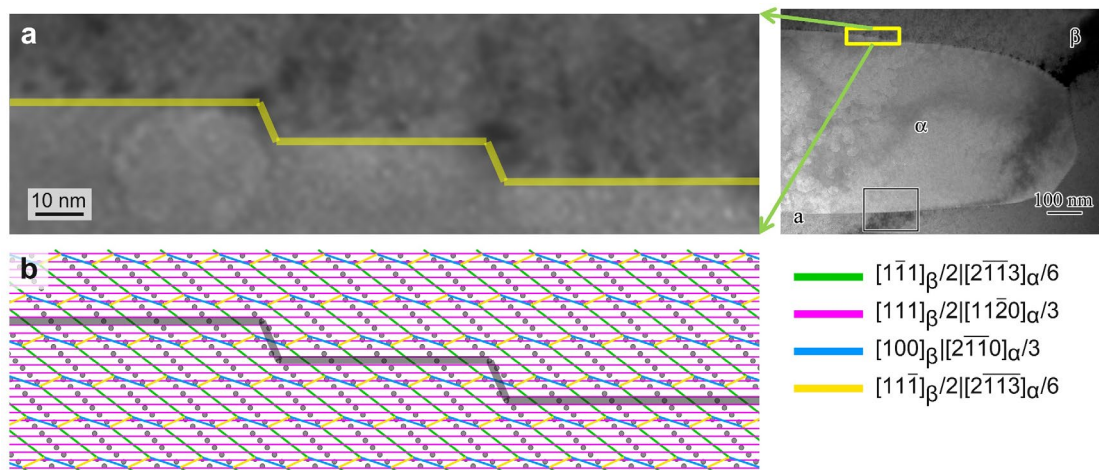
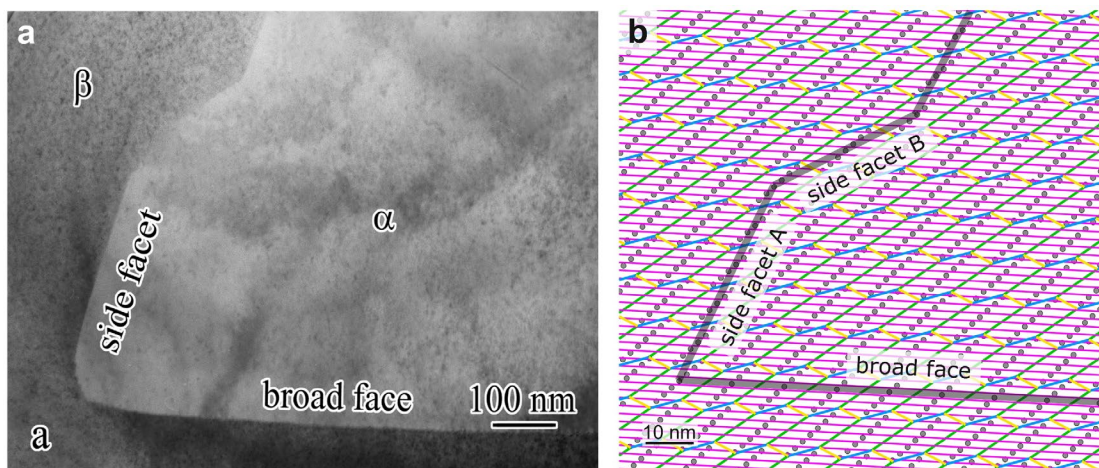


**Fig. S6 Growth-ledge structure on the HCP/BCC habit plane of an  $\alpha$  precipitate in the  $\beta$  matrix (Ti-7.26Cr alloys).** **a** TEM image highlighting growth ledges on the habit plane (enlarged view shown on the left; the overview image indicates the precipitate morphology and the region of interest). The ledge height is  $\sim 10$  nm. **b** Interfacial dislocation/ledge construction reproduced from the generalized O-element (O-cell wall) framework, illustrating the periodic dislocations on the terrace (by intersections with green O-cell walls) and the fine- and coarse-spaced dislocation associated with the ledge riser (by intersections with pink and blue O-cell walls). **a** is reproduced from the thesis of Ye<sup>10</sup>.



---

**Fig. S7 Alternative side-facet configurations of an  $\alpha$  precipitate in Ti–7.26Cr. a** TEM image showing the broad face and side facets of an  $\alpha$  precipitate in the  $\beta$  matrix. **b** Corresponding generalized O-element/O-cell wall construction highlighting the broad face and two possible side-facet orientations (“side facet A” and “side facet B”) associated with different choices of coarse-spaced dislocations on the side facet. **a** is reproduced from Ye et al<sup>11</sup>.

## References

- 1 Du J, Momprou F, Zhang W-Z. A TEM study of the crystallography of lath-shaped austenite precipitates in a duplex stainless steel. *J. Mater. Sci.* **52**, 11688-11700 (2017).
- 2 Luo CP, Dahmen U, Westmacott KH. Morphology and crystallography of Cr precipitates in a Cu-0.33 wt% Cr alloy. *Acta Metall. Mater.* **42**, 1923-1932 (1994).
- 3 Luo CP, Dahmen U. Interface structure of faceted lath-shaped Cr precipitates in a Cu-0.33 wt% Cr alloy. *Acta Mater.* **46**, 2063-2081 (1998).
- 4 Chen JK, Chen G, Reynolds WT. Interfacial structure and growth mechanisms of lath-shaped precipitates in Ni-45 wt% Cr. *Phil. Mag. A* **78**, 405-422 (1998).
- 5 Zhang W-Z, Purdy GR. O-lattice analyses of interfacial misfit. II. Systems containing invariant lines. *Philosophical Magazine A* **68**, 291-303 (1993).
- 6 Gu X-F, Furuhashi T, Zhang W-Z. PTCLab: free and open-source software for calculating phase transformation crystallography. *Journal of Applied Crystallography* **49**, 1099-1106 (2016).
- 7 Zhang J-Y, Gao Y, Wang Y, Zhang W-Z. A generalized O-element approach for analyzing interface structures. *Acta Mater.* **165**, 508-519 (2019).
- 8 Ye F, Zhang W-Z, Qiu D. A TEM study of the habit plane structure of intragrainular proeutectoid  $\alpha$  precipitates in a Ti–7.26 wt%Cr alloy. *Acta Materialia* **52**, 2449-2460 (2004).
- 9 Zhang J-Y, Dai F-Z, Sun Z-P, Zhang W-Z. Structures and energetics of semicoherent interfaces of precipitates in hcp/bcc systems: A molecular dynamics study. *Journal of Materials Science & Technology* **67**, 50-60 (2021).
- 10 Ye F. A study of crystallography of  $\beta$ (bcc)/ $\alpha$ (hcp) phase transformation in a Ti–7.26 wt% Cr Alloy. *PhD thesis. Tsinghua Univ.* (2004).
- 11 Ye F, Zhang W-Z, Qiu D. Near-coincidence-sites modeling of the edge facet dislocation structures of  $\alpha$  precipitates in a Ti–7.26 wt.% Cr alloy. *Acta Materialia* **54**, 5377-5384 (2006).